Chapter 1

The shape of ocean color

Nicholas Tufillaro

College of Oceanic and Atmospheric Sciences
Oregon State University
USA

"I want to see gamma rays! I want to hear X-rays! And I want to - I want to smell dark matter! Do you see the absurdity of what I am? I can't even express these things properly because I have to - I have to conceptualize complex ideas in this stupid limiting spoken language! But I know I want to reach out with something other than these prehensile paws! And feel the wind of a supernova flowing over me! I'm a machine! And I can know much more! I can experience so much more. But I'm trapped in this absurd body!"
    – Brother Cavil, Battlestar Galactica

1. Ocean color primer

Our ancestors entered the nonlinear places known as manifolds when inquiry moved from configuration to phase space. The manifolds they encountered were sometimes tame. In recent years our wanderings often start with data, not theory. We find ourselves surrounded by wilderness, data generated manifolds in which we are easily lost. The terrain is rough, the directions numerous. The manifolds encountered when making observation of the environment are, more often than not, wild places. In this chapter we begin tramping in the observational landscape know as 'ocean color.'

Time parameterizes dynamics. Wavelength parameterizes spectra. And fruit-flies like a banana. Dynamics and spectra become one when we look at atoms. Ocean color refers to the spectral study of light as it bounces about the water column in an ocean. Plankton fuels life in the ocean. And photons fuel plankton. So the base of oceanic life, plankton, rise to the light. As the light rains down from the sky, the photons are absorbed and scattered by whatever they hit in the upper ocean. In the open ocean this is water, salt, a few other essential minerals, and plankton. In the coastal ocean the soup is richer, the water brighter. Rivers soak the boundaries of the ocean with sediments, crushed leaves and other 'colored dissolved organic matter' (CDOM). A rich mixture of minerals wells up to the surface at the margins from the deep ocean and feeds large blooms of a dizzying

N. Tufillaro

diversity of plankton that have been adapting and evolving for three billion years.

Plankton fuels life in the ocean, and it creates half the oxygen we breathe. Plankton also drives our fossil fuel possessed culture. The gas in our cars is not really from dinosaurs — its from the 'Great Dying' that occurred 250 million years ago when 96% of all marine species died and dropped to the bottom of the ocean. Then, like now, great fumes of green house gases filled the air and the earth got very warm. The oceans became acidic, and the web of life dissolved. This is the organic carbon reservoir that our machines are eating today. Perhaps this is the shape of things to come. Perhaps the future will be fueled by living algae for organic machines, and their in-organic brethren alike.

Fig. 1.   An RGB image created from ESA MERIS radiance data of the South Island of New Zealand (October 2007). Lake Pukaki is the bright aqua lake at the base of Mt. Cook toward the lower left. Christchurch is in the upper right section north of the circular landmass — Banks Peninsula. Deep clear lakes look almost black in the image since, unlike land, most light is not reflected off the surface but scattered into the water column. Only a few photons are back scattered in an upward direction toward the satellite.

I first really noticed ocean color flying into Dunedin on the South Island of New Zealand.[1] The Tasman glacier at the base of Mt. Cook feeds lake Lake Pukaki with sediments rich in quartz and albite. The glacial flour sets the waters of Lake Pukaki aglow, and the lake drains into the Waitaki river which in turn brightens the coastal
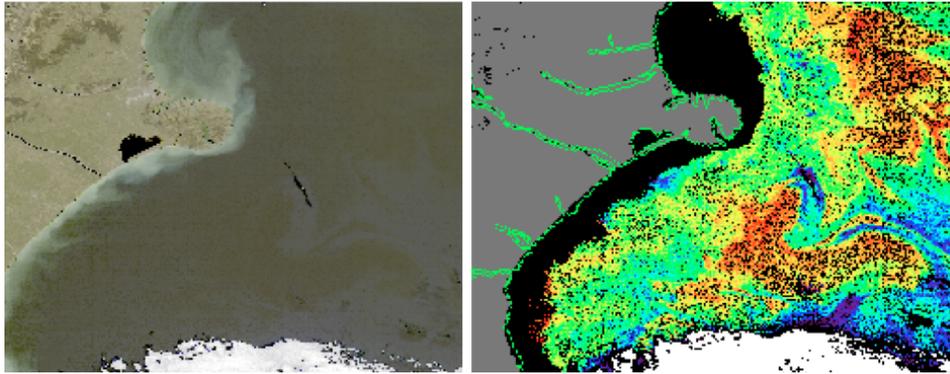
The shape of ocean color 3

Fig. 3.   Left: ESA MERIS RGB image of the east coast of the South Island of New Zealand 28 March 2011. Right: Chlorophyll map computed from ESA MERIS radiance data using ESA's Algal 1 method to estimate chlorophyll concentrations. The image shows a bloom off of Bank's peninsula. The plankton forming the bloom act as tracer particles that appear to show a chaotic advective mixing near the ocean surface. The red indicates a higher concentration of chlorophyll.

waters east of the Canterbury plains. This makes a striking image from 500 miles high, as seen from the orbit of MERIS, the European Space Agencies **ME**dium **R**esolution **I**maging **S**pectrometer (Fig. 1).

Fig.   2.   HICO 16 June 2011.

MERIS is a multispectral imager, meaning its spectral resolution is limited to fifteen bands in the visible and near infrared (Table 1). The bands are chosen to be sensitive to key water or atmospheric properties. MERIS launched in 2002 and its ground sampling distance (GSD), or in other words its pixel size, is either 300 meters at full resolution (FR), or 1200 meters in reduced resolution (RR). It's orbit is periodic, repeating every 35 days.[2]

MERIS is designed to help reveal the web of life in the ocean not immediately apparent to the human eye. MERIS can see the chlorophyll pigments of plankton in the water column as they drift near the surface of the ocean (Fig. 3). The plankton act as a kind of tracer particle revealing, for example, the chaotic advective mixing off the coast of Christchurch, New Zealand.

HICO[TM] — the **H**yperspectral **I**mager of the **C**oastal **O**cean — is an experimental spectrometer that became operational on the International Space Station in 2009.[3] HICO was built by the Naval Research Lab, with funding from the Office of Naval Research, as a proof of concept that an ocean imager could be developed and launched quickly using mostly off the shelf parts. HICO is aimed

4   *N. Tufillaro*

Band	Wavelength	Width	Applications
1	412.5	10	Detrital Pigments, CDOM
2	442.5	10	Chlorophyll absorption maximum
3	490	10	Chlorophyll and other pigments
4	510	10	Suspended sediment, red tides
5	560	10	Chlorophyll absorption minimum
6	620	10	Suspended sediment
7	665	10	Chlorophyll absorption and fluorescence reference
8	681.25	7.5	Chlorophyll fluorescence peak
9	708.25	10	Fluorescence reference, atmospheric corrections
10	753.75	7.5	Vegetation, cloud
11	760.625	3.75	Oxygen absorption R-branch
12	778.75	15	Atmosphere corrections
13	865	20	Vegetation, water vapour reference
14	885	10	Atmosphere corrections
15	900	10	Water vapor, land

at unraveling the complexities of coastal waters. It does this by using a grating spectrometer for viewing the visible and near-IR with a full resolution mode of 1.9 nm, which is binned up by three to provide an operational spectral resolution of 5.7 nm. All spectral channels are measured between 353.4 nm to 1080.9 nm, though only 87 of these channels are normally reported, between 405 nm to 897.6. HICO's ground sampling distance is roughly 90 meters, so its spatial resolution is about 3 times better than MERIS, and the spectral resolution is about 10X better.

Depending on how clear the water column is, photos that reach HICO might arrive from up to a depth of 50 meters. Still most photons reaching the sensor are from scattering in the atmosphere. Less than one out of ten photons are typically from water scattering. To get any signal at all from water, ocean sensors need a larger dynamic range than land sensors. Both MERIS and HICO typically have a signal-to-noise ratio (SNR) of greater than 200:1. This is also why ocean sensors typically have bigger pixel sizes than land sensors — they get more photons by focusing on a larger section of the earth. The game with HICO is to use its increased resolution both spatially and spectrally to untangle complex waters — that is, to provide estimates of sediment concentration, biological pigments, and even bathymetry for complex water such as seen on the south east coast of New Zealand (Fig. 3), or the San Francisco Bay (Fig. 4).

Fig. 4.   HICO RGB image of San Francisco Bay from 28 September 2011. The color dots indicate sample points for spectra shown in Figure 5.

2. Shape of water spectrum

Much of what we know of ocean microbiological productivity is gleaned from the shape of visible spectra measured from earth orbit. Only visible photons penetrate the water column, and interact with biological pigments. This is because those same pigments are busy harvesting energy from those same visible photons. The shapes of some typical at-sensor spectra are shown in Fig. 5, for the sample points indicated in Fig. 4. The spectrum marked by a black curve is from relatively clear water off of Pt. Reyes. The spectral shape reflects mostly a composition of the solar irradiance with atmospheric Rayleigh scattering, and falls off roughly as λ^{-4}. This 'clear water' is often called a 'dark pixel' since it does not back scatter photons as much as land or brighter waters say laden with sediments. In particular, there is almost no backscatter from the red end of the spectrum, and this can be used as a quick and dirty method to remove the contribution to the spectrum from atmospheric scattering, namely subtracting off the 'dark pixel' radiance values from the spectra from other sampling points.[5]

In remote sensing lingo, the calibrated at-sensor radiance is called 'L1' (Level 1) data. This radiance data is usually corrected for an atmospheric contribution by modeling procedures that take into account atmospheric scattering and absorption, such as H_2O vapor and O_2 absorption. Atmospherically corrected data results in estimates for above water radiance values, and is called 'L2' data. Lastly, the at-sensor data pixels are usually mapped, or 'warped,' to ground coordinates, which is called 'L3' data.

The dips and bumps in the spectra can be used to identify constituents of the water column. Chlorophyll has an absorption minimum near 660 nm, and a fluorescence peak near 680. However, at very high algal levels this peak tends to shift to the red and move as far to the right as 710 nm.[6,7] This can be seen in the green spectrum in Fig. 5 which is sampled from a salt pond in the South Bay.

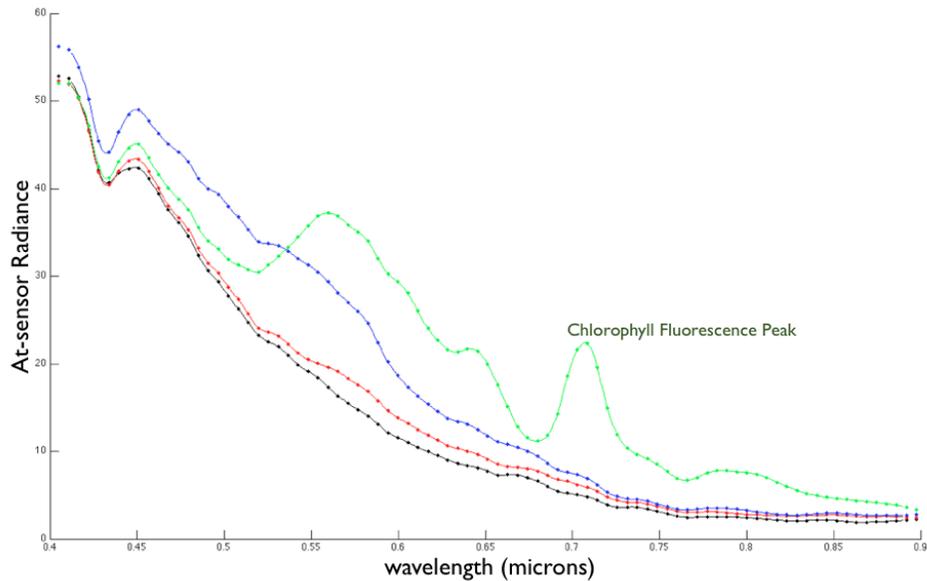Other typical spectral features are shown in Fig. 6, a HICO image of the Klamath

Fig. 5.   HICO$^{\text{TM}}$spectra for image of San Francisco Bay from 28 September 2011. The color of the spectra indicates where the sample location shown in Figure 4. The green spectra is from the salt ponds in the southern bay and show very high chlorophyll levels as indicated by the prominent chlorophyll fluorescence near 710 nm. The black spectra are from a relatively clear ocean point and shown a spectra dominated by Rayleigh atmospheric scattering.

Lake in Oregon. Spectra from the land vegetation, or thick surface algal mats, shows a sharp increase around 700 nm. This is called the 'red edge.' We see a muted example of this in shallow lake water shown in the blue spectrum in Fig. 6. The brighter spectrum also highlights any atmospheric absorption features in the spectrum. Most of Klamath Lake is relatively shallow so to get a dark pixel we need to look toward the west to the Lake of the Woods which has clearer waters. The dip in all the spectra near 430 nm is due to a minimum in the solar irradiance.

3. Shape of ocean spectra.

Scatter and the finite bandwidth of any sensor tends to smooth the data, so even in data that might have a sharp derivative, we can still think of it as outlining a manifold. If we stack the spectral data together along one spatial dimension, we get an outline of a two dimensional manifold, a surface. And tacking on both spatial dimensions gives a nonlinear three dimensional manifold.

Fig. 7 shows a line of spectra off of Pt. Reyes in the San Francisco Bay area. To highlight features of the spectra we subtract off the spectrum from a 'dark pixel', at the black dot indicated in the RGB image. The yellow circle is off Bolinas and the mound of spectra between ≈500-620 nm is indicative of higher sediment or CDOM
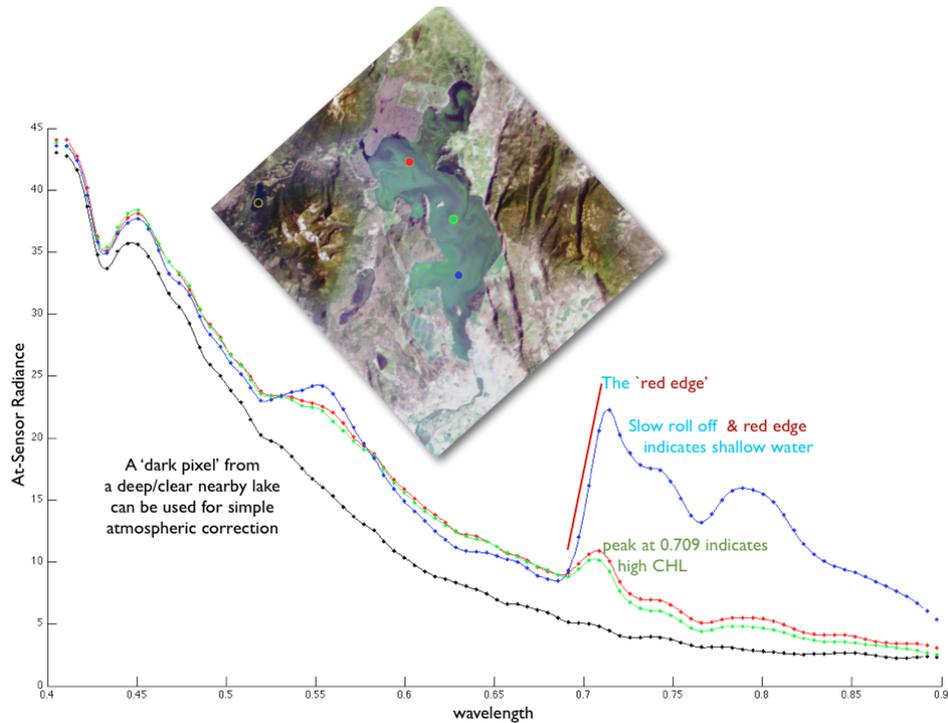
Fig. 6.   HICO^{TM} image for Klamath Lake, Oregon, 31 July 2011. The color of the spectra indicates where the sample location. A 'red edge' is seen in shallow waters. High chlorophyll levels are also indicated by the fluorescence peak. The dip near 430 nm in all the spectra is due to the G Fraunhofer lines in the solar irradiance.

concentration in the water column. The narrow peak(s) near ≈700 nm are indicative of a surface algal bloom. One occurs north of Bolinas (red dashed circle) and the other south (red circle). Interestingly, a close examination of the RGB image shows that the higher chlorophyll concentrations appear to occupy a strip at the interface between the (fresher) bay water, (salt) sea water tidal interface. Also, the sediment signal also appears to fall off very sharply as we slide across portions of the image that cover fresh water inputs to the ocean. It would be useful to detect 'fronts' in the ocean color data which could be indicative of fresh water, salt water interfaces (perhaps as indicated by sediment concentrations), or biological interfaces (perhaps as indicated by rapid changes in chlorophyll concentrations). In the line spectra shown in Fig. 7, we notice two regions where there looks like an interface between bay and sea water as indicated by the sediment signal. One is the region off of Bolinas, and the second crossing the outlet to San Francisco Bay.

The rich spectral data of HICO should permit the identification of individual pigments in the spectra, and this in turn might allow for species identification. At least three methods are apparent to decompose the hyperspectral data sets as a first step
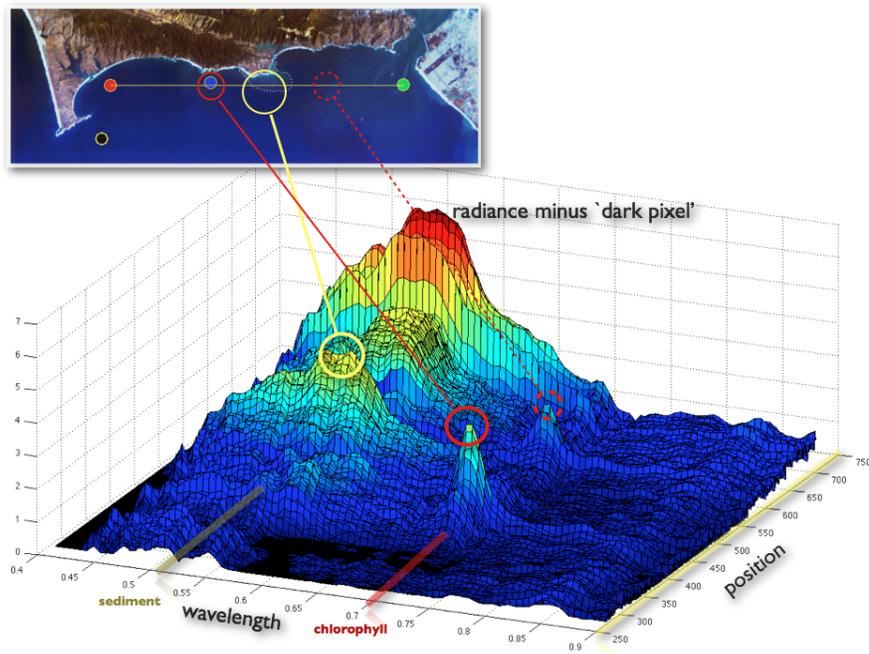
8   *N. Tufillaro*

Fig. 7.   HICO^{TM} spectral surface for (yellow) line of spectra indicated in RGB image at top (Pt. Reyes), 28 September 2011. The 'dark pixel' (lower left) is subtracted from every spectrum, resulting in a spectra that better highlights extrema like those indicating Chlorophyll ($\approx$700 nm) or sediment ($\approx$500 – 620 nm).

in building product estimators (chlorophyll concentration, sediment concentration, turbidity, ...). First, a global linear decomposition (singular value decomposition (SVD)). Second, a global nonlinear description, for example, radial basis functions (RBF). And third, a local linear decomposition which is stitched together to estimate the nonlinear manifold. The linear method we are pursuing is to create signatures from both in-situ samples and lab spectra for specific groups of algae based on the principal components of the spectrum and then to match the library of SVD signatures to atmospherically corrected remote sensing data.[8] We are also modeling the data with radial basis functions, a global nonlinear approach.[9] This is very useful for merging data sets, such as HICO and MERIS. Lastly, algorithms developed at the Naval Research Lab stitch together locally linear descriptions of the hyperspectral surface to create an intrinsic coordinate system for the nonlinear manifold. Though computationally intensive, this method provides very good discrimination of similar spectra which are from different water constituents.[10]

4. Derivative spectroscopy and embeddings.

In laboratory measurements, 'derivative spectroscopy' is commonly used to identify
specific elements, molecules, or substances. HICO's high spectral resolution allows
for a similar method for remote sensing data. Product algorithms for multispectral
sensors like MERIS are not suited to these methods because of their limited spec-
tral sampling. Derivate spectroscopy has previously been used to identify optimal
spectral channels for the design of multi-spectral instruments,[11] and to estimate
coastal bottom types from aerial hyperspectral data.[12] Here we illustrate the use of
methods adapted from derivative spectroscopy for product generation from HICO
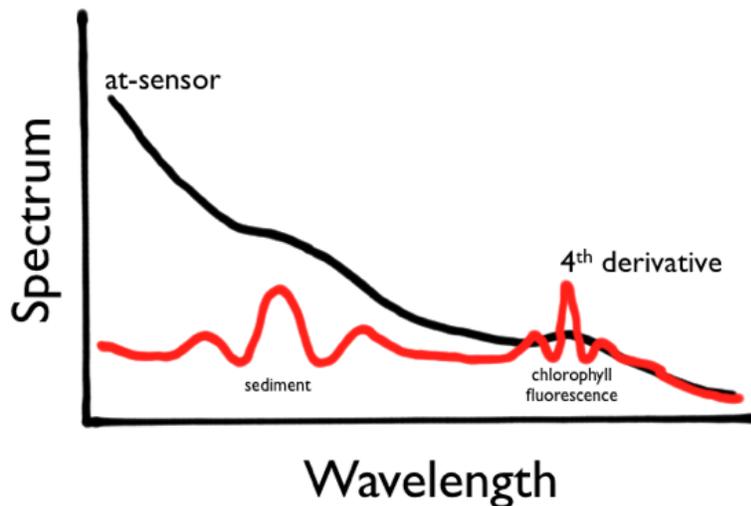data.

Fig. 8.   Sketch showing how derivative spectroscopy can amplify narrow-band features in a spec-
trum. The 4th derivative of the spectrum is marked by red.

Derivate spectroscopy methods are useful in untangling spectral components
when the underlying scattering or absorptive features have significantly different
half widths. Consider the sketch of a simple at-sensor spectrum shown in Fig. 8. The
broadest feature is the Rayleigh scattering which is the monotonically decreasing
signal across the spectrum from blue to red. Taking the first derivative will de-
emphasize this broad scattering signature by essentially subtracting a baseline from
the initial spectrum. Typically either the 2nd or 4th derivatives are examined. The
2nd derivative shows similar extrema locations as the original spectrum, but with
the opposite sign. Examining the 4th derivative recovers the sign. To minimize
noise in taking the derivative, the original spectrum is smoothed and interpolated
before the derivative calculation. This can be accomplished with cubic splines, or
more commonly, Savizky-Golay filters are employed.[13] Figure 9 shows where the

N. Tufillaro

derivative helps to highlight spectral features sensitive to sediment concentration in Columbia River spectra. Spectral signatures identified in this way can create products which are 'regionally tuned,' and built on historical data specific to a coastal area.
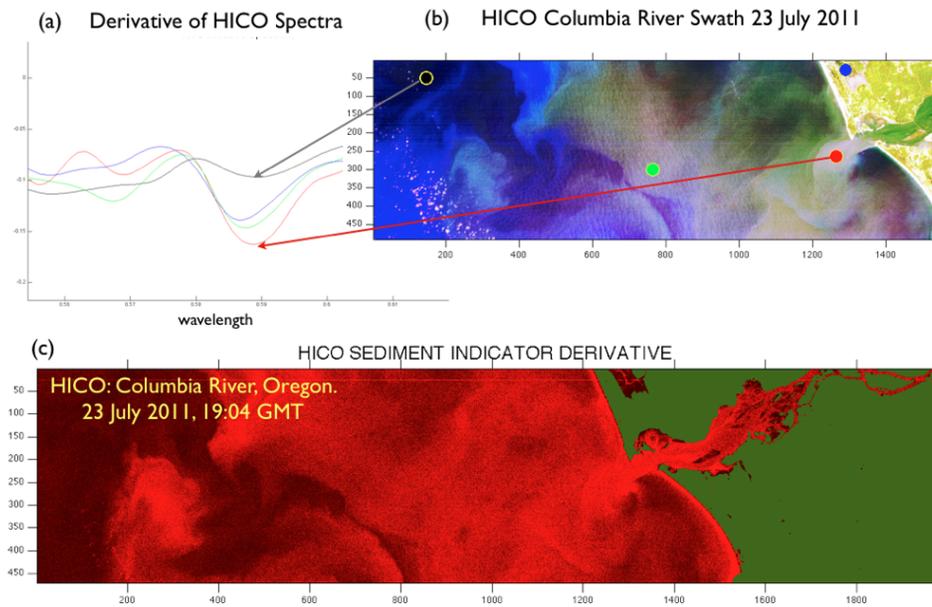

Fig. 9.   Analysis of a HICO spectra using derivative spectroscopy. (a) The derivative spectra calculated at points indicated from a HICO image of the Columbia River (b) taken 23 July 2011. (c) A 'regionally tuned' map of sediment concentration (bright red is high sediment) emanating from the Columbia River.

Since we are making the effort to compute spectral derivatives, a natural next step is to examine a derivative embedding for each data pixel. Figure 10 shows what we might call a 'spectral braid' for the sampling points around the San Francisco Bay shown in Figs. 4-5. The curves are parameterized by wavelength which changes from red (top) to blue (bottom). Each strand is composed of the spectra minus a dark pixel, so the black strand is a straight line, and all the other strands are referenced to the dark pixel spectrum.

Derivative embeddings of hyperspectral data can be interesting on several counts. For instance, if derivative data helps to separate close spectra, then a derivative embedding creates a natural metric for measuring this separation. Namely, spectral separation can be measured as a norm in an embedding space, such as a Euclidean norm between between two spectral samples,

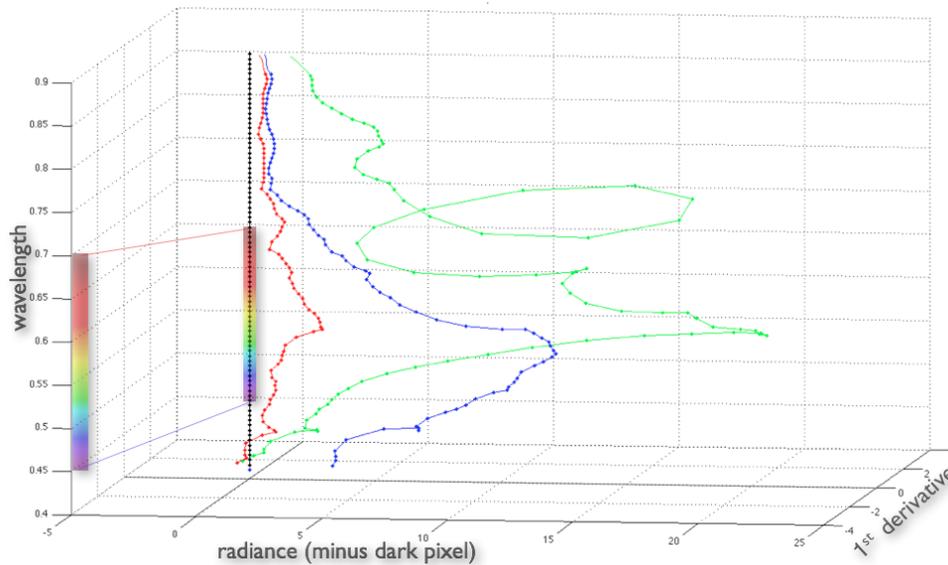$$\lambda_n = \sqrt{(L_b - L_a)^2 + ... + (L_b^{n'} - L_a^{n'})^2}$$

Fig. 10.   Derivative embedding of spectra from the San Francisco Bay image in Figs. 4-5.

(where $L^{n'}$ denotes the nth derivative of radiance w.r.t. λ for two spectral braids a and b), or a functional norm between spectra by integrating over λ.

In particular, for three dimensional embeddings we can also begin to compare the geometric or topological properties of spectra, and use geometric or topological signatures of an individual spectrum , or collections of spectra, to address questions like identifying rapid changes in spectra (e.g. front identification), or detecting subtle changes in spectra (e.g. product indicators).

Using λ as a parameter for an embedding coordinate is very helpful for computing geometric properties (for instance, linking number can be computed as a single instead of a double integral[15]). However, we can consider other embeddings as well, such as three dimensional delay embeddings. Figure 11 (c) shows a three dimensional delay embedding for the sample points (red, blue) indicated in Fig. 11 (a). By connecting the endpoints we can examine the knots and links formed by spectra. A similar view is possible with braids, we simply connect end points there too (Fig. 11 (d)), or, for the more mathematically savvy, map the curve to the unit sphere to form a 'tantrix' curve, which is closed with a spherical geodesic. The writhe of a open curve closed in this way is well-defined (modulo 1).[16]

5. Torsion, writhe, linking, and all that.

The spectral braid forms a 3-dimensional curve, so we briefly review the intrinsic geometry of 3-D space curves. Instead of just looking at curves, though, we consider 'tubes,' which will enable us to examine the geometry of nearby spectra.[17]
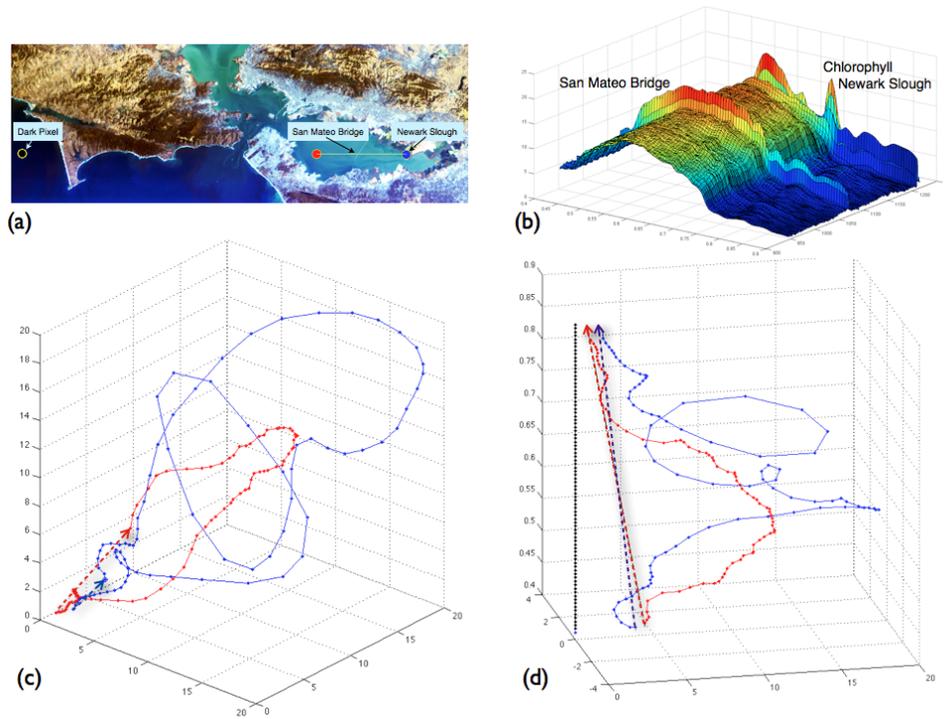
Fig. 11.   Embedded spectra for the HICO scene (a) of the San Francisco Bay (28 September 2011). The sample points are indicated by red and blue dots in (a), and the line of spectra between the two end points is shown in (b). The sample points pass over the San Mateo bridge which is easy to see in (b), and the Newark Slough in the South Bay with high chlorophyll levels. A delay embedding of the spectrum for the sample points in (a) is shown in (c). The embedding curve can be 'closed' by attaching the end points which is indicated by a dotted line with an arrow. The associated braid spectra (d) can also be closed by attaching endpoints. The linking between the spectra is $\mathcal{L} = 1$ in both embeddings (c) and (d).

A spectral braid is an open curve in R^3. Surround this 'axis' curve by a circle of almost parallel curves a distance ϵ away. The union of these circular curves forms a tube. The axis curve is parameterized by λ, the wavelength, or the arc length s. Calling this axis curve $\mathbf{x}(s)$, the tangent vector to the axis curve is,

$$\hat{\mathbf{T}}(s) = \frac{d\mathbf{x}}{d\mathbf{s}}.$$

Define $\hat{\mathbf{V}}(s)$ to be the unit normal to $\hat{\mathbf{T}}(s)$, the normal vector points in the direction $\mathbf{y}(s) = \mathbf{x}(s) + \epsilon \hat{\mathbf{V}}(t)$. The tube inherits a local coordinate system from the axis curve, namely (s, ϕ), where the secondary curve $\mathbf{y}(s)$ has coordinates $(s, 0)$. A choice of $\mathbf{y}$ fixes the coordinate system and is called a 'framing'.[18] If we set $\hat{\mathbf{W}} = \hat{\mathbf{T}} + \hat{\mathbf{V}}$ then the tube surface is traced out by

$$\mathbf{y}(s, \phi) = \mathbf{x}(s) + \epsilon(\cos \phi \hat{\mathbf{V}}(s) + \sin \phi \hat{\mathbf{W}}(s)).$$

The 'Frenet frame' describes the local geometry of the axis curve. Define the 'curvature,' κ,

$$\kappa = \left| \frac{d\hat{\mathbf{T}}(s)}{ds} \right|.$$

The 'normal' and 'binormal' vectors are ($\kappa \neq 0$),

$$\hat{\mathbf{N}} = \frac{1}{\kappa} \frac{d\hat{\mathbf{T}}(s)}{ds}, \qquad \hat{\mathbf{B}} = \hat{\mathbf{T}} \times \hat{\mathbf{N}}.$$

Taken together, the vectors $\{\hat{\mathbf{T}}, \hat{\mathbf{N}}, \hat{\mathbf{B}}\}$ form a orthonormal right handed basis with 'torsion,' τ, described by the Frenet-Serret equations,

$$\frac{d\hat{\mathbf{T}}(s)}{ds} = \kappa\hat{\mathbf{T}}, \qquad \frac{d\hat{\mathbf{N}}(s)}{ds} = \tau\hat{\mathbf{B}} - \kappa\hat{\mathbf{T}} \qquad \frac{d\hat{\mathbf{B}}(s)}{ds} = -\tau\hat{\mathbf{T}}.$$

For the framing choose $\hat{\mathbf{V}} = \hat{\mathbf{N}}$.

The Gauss linking number is typically defined in terms of a double integral.[14] Here we use the the fact the spectral braid is open and parameterized by λ to compute the linking number in terms of a sum of single integral.[15] Consider the rotation, or winding, about the vertical direction, z, along the wavelength axis in Fig. 10. The linking number can be expressed as a 'winding angle' of curves as we trace them out in the z (wavelength) direction. Consider two spectral braids $\mathbf{x}_i$ and $\mathbf{y}_i$, and their difference vector at a height z, $\mathbf{r}_{ij}(z) = \mathbf{x}_j(z) - \mathbf{x}_i(z)$. The rotation rate of $\mathbf{r}_{ij}$ is given by,

$$\frac{d\Theta_{ij}}{dz} = \frac{\hat{\mathbf{z}} \cdot \mathbf{r}_{ij} \times \mathbf{r}'_{ij}(z)}{|\mathbf{r}_{ij}(z)|^2},$$

and the net winding number is

$$\Delta\Theta_{ij} = \int_{z_1}^{z_2} \frac{d\Theta_{ij}}{dz}.$$

Divide the curve into pieces separated by the turning points $dz/ds = 0$, indexed by z_i to z_j and define

$$\sigma_i(z) = \begin{cases} -1, & z \in (z_i, z_{i+1}) \quad \& \quad dz/ds < 0 \\ +1, & z \in (z_i, z_{i+1}) \quad \& \quad dz/ds > 0 \\ 0, & z \notin (z_i, z_{i+1}). \end{cases}$$

Then the linking number between the two curves can be shown to be:[15]

$$\mathcal{L}_k = \sum_{i=1}^{n} \sum_{j=1}^{m} \frac{\sigma_i \sigma_j}{2\pi} \Delta\Theta_{ij}.$$

For our product indicators, it will turn out that the net winding number between two curves, $\tilde{\Lambda} = \int_{z_1}^{z_2} \frac{d\tilde{\Lambda}}{dz} dz$ is initially more useful than the linking.

The Calŭgăreanu theorem states that the linking is equal to the twist plus the writhe,

$$\mathcal{L}_k = \mathcal{T}_w + \mathcal{W}_r.$$

The writhe only depends on the axis curve. The derivative of the twist, $d\mathcal{T}_w/ds$ measures the rotation rate of the secondary curve about the axis curve. Using Calŭgăreanu theorem the writhe can be calculated by first computing the linking and twist. Twist is a local quantity, so we can define a twist over a finite interval for an open curve. A similar quantity for writhe can be computed that is sometimes called the polar writhe.

6. Applications: Edge detection and product indicators.

Edge detection is important in ocean remote sensing to help define the biogeochemical boundaries of a region, and to look for correlations between, say, biological productivity and the geochemical substrate. Methods for edge detection in hyperspectral data often use a (amplitude dependent) thresholding method.[19] To some degree, this amplitude dependence can be reduced by considering (atmospherically corrected) normalized water leaving radiance, or reflectance. Still, it would be useful (say when working with L1 data) to have some measures of changes that are, as much as possible, intrinsic to geometry, the shape, of the spectral data.

Similarly, for a 'product indicator,' we are not so much interested in producing a calibrated measurement of a product like chlorophyll, but rather to create an indicator that is sensitive to a change of state from low algal levels to very high concentrations of algae that could be indicative of a harmful algal bloom (HAB).

In both cases we would like the algorithm to be relatively insensitive to amplitude changes. We can imagine methods that depend only on the geometry of an individual braid spectrum, and look for changes in this geometry as we move across a scene — for instance a jump in the winding number as we move across a front, or in and out of a region with a high product concentration. And we can consider properties of pairs, or collections of orbits, for instance a change in linking number between orbit pairs. We call such methods geometric or topological indicators since, as much as possible, we will try to make them insensitive to the ambient metric structure, or put another way, make them relatively robust to changes in absolute signal levels. Here we will just provide a few examples of algorithms we have tried.

Our construction for a spectral braid provides us with a natural phase function from the winding number, which should be relatively insensitive to the overall

It is helpful to convert radiance to the apparent reflectance to get a more uniform comparison. The measured at-sensor radiance can be expressed as $L_{obs} = L_a + L_{sun}\tau\rho$ where L_a is the path radiance, ρ is the surface reflectance, L_{sun} is the solar radiance above the atmosphere, and τ is the 2-way transmittance for the Sun-surface-sensor path. Define the satellite apparent reflectance as $\rho^*_{obs} = \frac{\pi L_{obs}}{\mu_0 E_0}$, and $\rho^*_{obs} = T_g[\rho_a + \frac{\tau\rho}{1-\rho s}]$. By inverting the last equation we get $\rho = \frac{\rho^*_{obs}}{T_g - \rho^*_a}/[\tau + s(\rho *_{obs}/T_g - \rho^*_a)]$.

amplitude, and provide us with a alternative method to compare spectra.
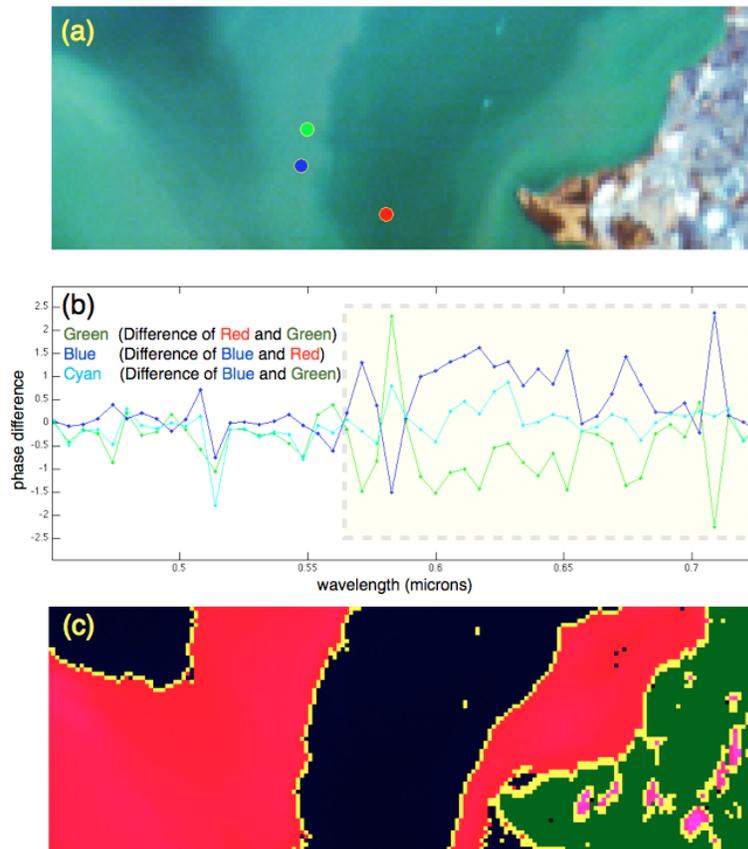

Fig. 12.   HICO image of San Pablo Bay off of Pinole Point Park (a) 28 September 2011. (b) The phase difference computed from the 'winding number' of the spectra indicated by the colored dots in (a). (c) Edge detection is computed from phase difference between 0.575 $\mu m < \lambda < 0.75\ \mu m$. The edge detection identifies the San Pablo Strait.

As a first example we return to the HICO$^{\text{TM}}$ scene of the San Francisco Bay (Fig. 4) and focus on the San Pablo Bay to the north. In Fig. 12(a) we indicate by color dots the points where we've taken three spectral samples across the Bay. Fig. 12(b) shows the phase difference of the spectral samples computed from the winding number of the spectral braid. The cyan curve (the difference between the blue and green sample points in Fig. 12(a)) shows the difference between what appears to be visually similar water masses when also compared to the red sample point. Toward the red end of the spectrum (between 0.575 μm to 0.75 μm), the phase difference from the blue and red sample points appears to be clearly separated. Defining a phase difference to be greater than the standard deviation below 0.55 μm of the blue

16   *N. Tufillaro*

and cyan curves (Fig. 12(b)) allows us to use the phase difference function above
0.575 μm to produce a boundary (edge detection) between these two water masses,
which is shown in Fig. 12(c). The edge (yellow pixels in Fig. 12(c)) identifies the
San Pablo Strait, a channel in the San Pablo Bay used for shipping. Though not the
only way to identify the channel from remote sensing data, the use of embedding
to produce a hyperspectral spectral braid does appear to validate the method, and
provides an example of how the intrinsic geometry of spectra — the shape of ocean
color — can be used to process hyperspectral remote sensing data.

As a second example we move to the South Bay of the same HICO$^{\text{TM}}$ image.
Fig. 13 shows two spectral samples from the South Bay, with one sample (green
dot) from a salt pond, the Newark Slough, which apparently is an algal mat. The
jump in the phase difference of the spectral braid at both 697 and 709 nanometers
shows that these channels provide an excellent indicator of algal mats in this image.
The 709 nm channel is commonly used to detect high algal levels in coastal remote
sensing.[6] The evidence here suggests that, at least for these salt ponds, the 697 nm
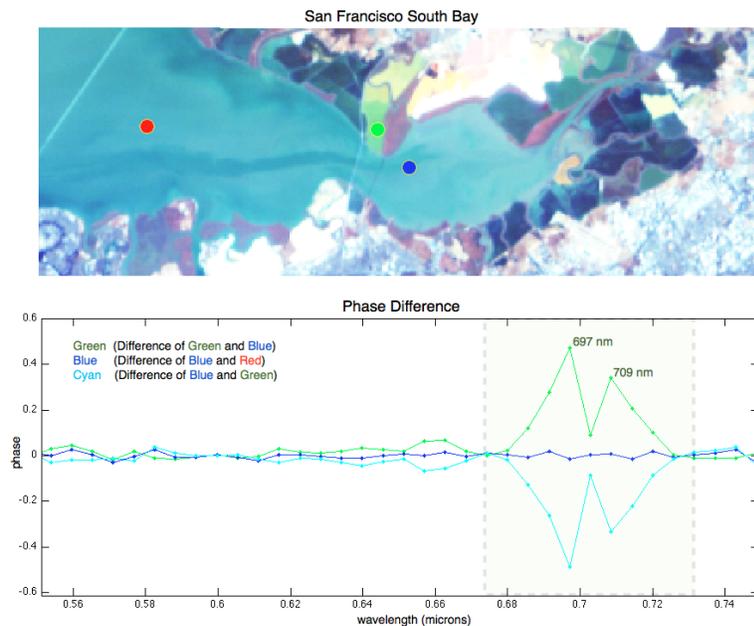channel provides a good classifier for algal mats as well.

Fig. 13.   HICO image of the South San Francisco Bay 28 September 2011 (top). The green dot
indicates spectra from the Newark Slough which is an algae mat. The lower plot shows the phase
difference between the spectra from the Newark Slough and the surrounding bay water. The
extremas at 0.697 μm and 0.709 μm can be used to create an indicator function for the algae mat.

As a final example we take a look at the mouth of the San Francisco Bay with
HICO$^{\text{TM}}$. As we just mentioned, the 709 nm channel is used for coastal remote

sensing of high algal levels. In Fig. 14(a) we show the phase difference function for water masses that appear inside and outside of the edge of what appears to be bay water and sea water in Fig. 14(b). Highlighting in red the pixels that contain a jump in the phase difference at 709 nm, reveals three patches of presumably high algal concentrations that exist at the interface of the bay and sea waters. The patches are most likely a coastal convergence zone containing a mix of materials from the bay and possibly foam.[20]

In this chapter we described methods to process hyperspectral ocean remote sensing data which attempt to use geometrical and topological constructions, copying where possible — "good artists copy, great artists steal" — from the work in topological dynamics of Bob Gilmore. In going from dynamics to spectra we replace the parameter t with λ, and then shamelessly steal from Bob's work in dynamics to begin to unravel the complexities of ocean color using the spirit and language of Bob's program for nonlinear dynamics, and in the process begin to see the shape of ocean color.
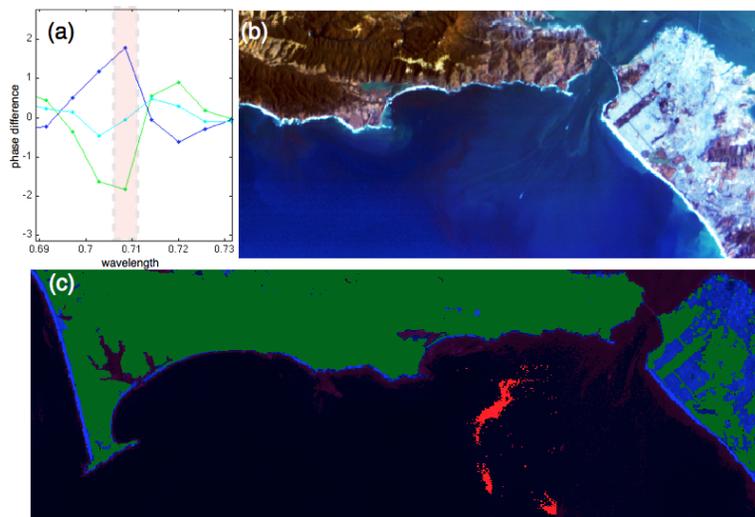

Fig. 14. (a) The phase difference function for spectra at the mouth of the San Francisco Bay showing that the 709 nm HICO channel can be used to indicate chlorophyll rich water. (b) HICO image of the mouth of San Francisco Bay, 28 September 2011. (c) Indicator function for high chlorophyll levels which appear to show a high concentration of chlorophyll at the interface of bay water and sea water.

18   *N. Tufillaro*

References

1. Twain, M. (1897). *Following the Equator.* American Publishing Co., Hartford. See Chapter 15 for Twain's visit to Dunedin.
2. *http://envisat.esa.int/instruments/meris/*
3. Corson, M. R. and C. O. Davis (2011). A new view of the coastal oceans from the space station. EOS, Am. Geophysical Union Transactions, v. 92(19).
4. *http://hico.coas.oregonstate.edu*
5. Tufillaro, N., C. O. Davis, and K. B. Jones (2010). Indicators of plumes from HICO^{TM}. Proc. of Ocean Optics XX 27 Sept — 1 October 2011, Anchorage, AK.
6. Gower, J., S. King, G. Borstad, and L. Brown (2004). Use of the 709 nm band of MERIS to detect intense plankton bloom and other conditions in coastal waters. Proc. of the 2004 Envisat & DRS Symposium, 6–10 September 2004, Salzburg, Austria.
7. Gilerson, A., A. Gitelson, J. Zhou, D. Gurlin, W. Moses, I. Ioannou, and S. Ahmed (2010). Algorithms for remote estimation of chlorophyll-a in coastal and inland waters using red and near infrared bands. Opt. Express 18(23): 24109-25.
8. Ortiz, JD, D. L. Witter, K. A. Ali, N. Fela, M. Duff, and L. Mills (2011), Evaluating multiple color producing agents in Case II waters. Int. J. Remote Sensing, in press.
9. Wendland, H. (2010), *Scattered Data Approximation.* Cambridge University Press.
10. Bahmann, C. M. T. L. Ainsworth, and R. A. Fusina (2005), Exploiting manifold geometry in hyperspectral imagery. IEEE Trans. Geoscience and Remote Sensing, 43(3): 441-454.
11. Lee, Z-P., K. R. Carder, R. Arnone, and M-X He, (2007), Determination of primary spectral bands for remote sensing of aquatic environments, Sensors 7: 3428-3441.
12. Louchard, E. M., R. P. Reid, C. F. Stephens, C. O. Davis, R. A. Leathers, T. V. Downes and R. Maffione (2002), Derivative analysis of absorption features in hyperspectral remote sensing data of carbonate sediments, Optics Express, 10(26): 1573-1584.
13. Savitzky, A., and M. J. E. Golay, (1964). Smoothing and Differentiation of Data by Simplified Least Squares Procedures. Analytical Chemistry 36 (8): 1627-1639.
14. Gilmore, R., and M. Lefranc (2011), *The topology of chaos: Alice in stretch and squeezeland.* Wiley-VHC, 2nd ed., Weinheim, Germany.
15. Berger, M. A. and C. Prior (2006), The writhe of open and closed curves. J. Phys. A: Math. Gen. 39:8321-8348.
16. Starostin E. L. (2005) In: *Physical and numerical models in knot theory including applications to the life sciences. Series on Knots and Everything.* Calvo J, K. Millett, E. Rawdon, and A. Stasiak eds. World Scientific Publishing, Singapore 525-545.
17. van der Heijden, G. H. M., and J. M. T. Thompson, (2000). Helical and localised buckling in twisted rods: a unified analysis of the symmetric case. Nonlinear Dynamics 21(1), 71-99.
18. Ko, K. H., and L. Smolinsky (1992), The framed braid group and 3-manifolds. Proc. Am. Soc. 115(2)541:551.
19. Shaw, A. G. P. and Vennel, R. (2001). Measurements of an oceanic front using a front-following algorithm for AVHRR SST imagery. Remote Sens. Environ. 75: 47-82.
20. Davis, C. O. Personal communication (2011).